

Article

Novel Mixed-Phase α/γ -Fe₂O₃ Micro-Flower Assembled with Nanosheets for Enhancing Acetone Detection

Ruonan Tian¹, Huai Tan¹, Gang Chen¹, Hongtao Guan¹ , Chengjun Dong^{1,2,*} and Zongyou Yin^{2,*} ¹ School of Materials and Energy, Yunnan University, Kunming 650091, China² Research School of Chemistry, Australian National University, Canberra, ACT 2601, Australia

* Correspondence: dongcj@ynu.edu.cn (C.D.); zongyou.yin@anu.edu.au (Z.Y.)

Abstract: Although individual γ -Fe₂O₃ and α -Fe₂O₃ have been widely fabricated for gas sensors, their mixed phase of α/γ -Fe₂O₃ might deliver excellent sensing properties. In this study, a facile solvothermal method was used to fabricate Fe-alkoxide. After thermal treatment, it was converted into γ -Fe₂O₃, α -Fe₂O₃ and their mixed-phase α/γ -Fe₂O₃ with a nanosheets-assembled flower-like structure. We studied the influence of calcination temperature on the phase and sensing properties on acetone detection. The α/γ -Fe₂O₃ which annealed at 400 °C included 18% α -Fe₂O₃ and it exhibited excellent sensing performance towards acetone compared to that of γ -Fe₂O₃ and α -Fe₂O₃. It showed a response of 353 to acetone with a concentration of 200 ppm, and a low limit of detection of 0.5 ppm at 160 °C. In addition, the change in responses with acetone concentration from 50 to 200 ppm shows a good linear relationship. Moreover, this material has good reproducibility and selectivity as well as a fast response time of 22 s and recovery time of 14 s to 200 ppm. Therefore, our mixed phase of α/γ -Fe₂O₃ possesses great prospects for acetone detection.

Keywords: Fe₂O₃; phase; gas sensor; acetone; sensing performance



Citation: Tian, R.; Tan, H.; Chen, G.; Guan, H.; Dong, C.; Yin, Z. Novel Mixed-Phase α/γ -Fe₂O₃ Micro-Flower Assembled with Nanosheets for Enhancing Acetone Detection. *Crystals* **2023**, *13*, 810. <https://doi.org/10.3390/cryst13050810>

Academic Editor: Arcady Zhukov

Received: 29 March 2023

Revised: 6 May 2023

Accepted: 8 May 2023

Published: 13 May 2023



Copyright: © 2023 by the authors. Licensee MDPI, Basel, Switzerland. This article is an open access article distributed under the terms and conditions of the Creative Commons Attribution (CC BY) license (<https://creativecommons.org/licenses/by/4.0/>).

1. Introduction

As a typical volatile organic compound (VOC), acetone is a generally used chemical reagent in the industry of paints, plastics, coating, laboratories, pharmaceuticals, and so on. However, acetone easily evaporates into the atmosphere, which risks human beings to undergo irreversible damage to physical health even at ppb-level concentrations [1]. In addition, the acetone concentration in respiratory gases of diabetic persons (over 1.8 ppm) is higher than those healthy individuals in the range of 0.3–0.9 ppm [2,3]. The effective acetone detection is used for diabetes diagnoses with the advantages of being non-invasive and painless. Hence, it is very necessary to construct a dependable gas sensor to quickly detect acetone with high performance and low cost. Significantly, chemoresistive gas sensors constructed from metal oxide semiconductors (MOSs) are greatly favorable [4]. Iron oxide (Fe₂O₃), as a kind of n-type MOS, is quite promising in the gas-sensing field [5]. So far, many approaches have been proposed to boost the sensing properties of Fe₂O₃, such as the regulation of morphologies [6,7], design of heterojunctions [8–10], doping of elements [11,12], functionalization of noble nanoparticles [13,14] and exposure of high-energy crystal facets [15–17]. However, another convenient method of adjustment of the crystalline phase is worth a try. For instance, Zhang's group discussed the relationship of the In₂O₃ crystalline phase and sensing properties with ozone, in which they found that the cubic bixbyite-type exhibited an extraordinary ozone-sensing performance [18]. It was reported that SnO₂ with a microstructure of nanorods and tetragonal and orthorhombic phases showed better sensitivity to detect isopropanol gas [19]. Wand and co-authors converted a metal organic framework into α -Fe₂O₃, γ -Fe₂O₃ and their mixed phase for n-butanol detection, in which the α -Fe₂O₃-based sensor exhibited the best sensing performance [20]. Therefore, it is extremely desirable to explore the effects of the Fe₂O₃ phase with a unique microstructure for acetone detection.

Usually, Iron oxide (Fe_2O_3) shows four crystal phases which are α - Fe_2O_3 , ϵ - Fe_2O_3 , β - Fe_2O_3 and γ - Fe_2O_3 . Among them, α - Fe_2O_3 with various microstructures has been extensively studied for different applications [21]: gas sensors in particular. Very recently, studies showed that γ - Fe_2O_3 is a potential candidate for gas sensors as well. However, α - Fe_2O_3 [22,23] and γ - Fe_2O_3 [24,25] have been studied separately for the application of gas sensors, which motivates us to synthesize Fe_2O_3 with different crystalline phases by a special precursor for acetone detection. The precursor will impact on the formation of a certain phase of Fe_2O_3 . Apart from the general precursors of MOF [26] and FeOOH [27], the iron alkoxides coordinated with metal ions based on hydroxyl groups of alcohols are a good alternative to fabricate Fe_2O_3 through thermal treatment [28]. In this study, an Fe-alkoxide precursor was first synthesized under assistance of ethylene glycol using a solvothermal method. Then, the Fe-alkoxide was converted into Fe_2O_3 and the influences of annealing temperature on phases were studied. The gas-sensing investigation demonstrated that the mixed phase of α/γ - Fe_2O_3 exhibited better sensing performance than that of single α - Fe_2O_3 and γ - Fe_2O_3 for acetone detection. Moreover, the potential sensing mechanism is discussed in detail with respect to the unique microstructure and the mixed phases of α/γ - Fe_2O_3 .

2. Experimental Section

2.1. Material and Chemicals

Ferric chloride ($\text{FeCl}_3 \cdot 6\text{H}_2\text{O}$), hexadecyl trimethyl ammonium bromide (CTAB), urea and ethylene glycol (EG) were purchased from Shanghai Aladdin Bio-Chem Technology Co., Ltd. (Shanghai, China), and used without further purification.

2.2. Synthesis of Hierarchical Fe_2O_3 Micro-Flower

Firstly, the Fe-alkoxides were synthesized by a one-step solvothermal route. Typically, 2 mmol $\text{FeCl}_3 \cdot 6\text{H}_2\text{O}$ and 3 g urea were dissolved into 100 mL of EG solution. Then, 1 g CTAB was added to obtain a homogeneous solution with stirring for 0.5 h. The solution was transferred to a 200 mL conical flask and refluxed in an oil bath at 180 °C for 30 min with vigorous stirring. When it cooled down naturally, green precipitates were rinsed with ethanol for three times, and dried in an oven at 60 °C for 12 h. The precursor was annealed at 350 °C, 400 °C and 450 °C for 2 h in air to prepare Fe_2O_3 . The as-prepared samples after annealing were red in color, which are named as α - Fe_2O_3 -350, α/γ - Fe_2O_3 -400 and γ - Fe_2O_3 -450, respectively.

2.3. Materials Characterization

X-ray diffraction (XRD) measurements were taken on Rigaku TTRIII with a $\text{Cu-K}\alpha$ radiation source. The scanning speed was set to 0.1°/min with a step of 0.02° from a 2 θ range of 10–90°. Field emission scanning electron microscope (FESEM) images were observed on a FEI QUANTA 200 microscope (USA) instrument at an accelerating voltage of 10 kV. Transmission electron microscopy (TEM) analysis was performed on a JEM-2100 (JEOL Ltd., Tokyo, Japan) microscope. The thermogravimetric analysis (TGA) was performed for Fe-alkoxides from room temperature to 800 °C in air with a heating rate of 10 °C/min using an American TA SDT-2960 thermal analyzer. Nitrogen adsorption-desorption isotherms were measured in a Micrometric ASAP 2010 automated adsorption analyzer. The materials were pre-outgassed in a vacuum at 300 °C for 2 h before nitrogen adsorption at 77.3 K. We used the Barrett–Joyner–Halenda (BJH) method to calculate the distribution of pore size. The chemical compositions of the sample were characterized by X-ray photoelectron spectroscopy (XPS) (Thermo Scientific Corporation, Waltham, MA, USA). All spectra were calibrated with C 1s peak at 285.0 eV.

2.4. Fabrication and Testing of Gas Sensor

Following our previous procedures [29,30], the gas sensors were fabricated. At the very beginning, a homogeneous paste was formed by mixing 0.1 gas-synthesized powder

with 0.2 mL deionized water. Then, the paste was coated on a 4 mm alumina ceramic tube. The thickness of the sensing layer was around 2 μm . Two Au electrodes were deposited at each end of an alumina ceramic tube, which was connected by Pt wires. Next, the resulting sensors were sintered at 350 $^{\circ}\text{C}$ for 2 h to facilitate good contact between the Au electrode and sensing material. Subsequently, a Ni–Cr coil heater was inserted into the alumina tube to provide the operating temperature through the heating current. Figure 1b shows the basic testing principle with the heating voltage (V_h), load resistance (R_L), export voltage (V_{out}) and working voltage (V_C). Finally, a base was used to connect the alumina tube and Ni–Cr heater to form a complete sensor unit, as shown in Figure 1c. A WS-30 gas-sensing measurement system provided by Weisheng Instruments Co. (Zhengzhou, China) (Figure 1a) with a test chamber of 18 L was used to measure and record sensing properties. According to the following static liquid gas distribution method, the amount of organic liquid was calculated and injected into the test chamber. After being evaporated, the vapor was mixed with air to form VOC gas with a desirable concentration.

$$C = (22.4 \times \rho \times d \times V_1) / (M \times V_2) \quad (1)$$

where C (ppm), ρ (g/mL) and d represent the gas concentration, density of the liquid, and purity of the liquid. In addition, V_1 (L), V_2 (L) and M correspond to the volume of the chamber and molecular weight of the liquid, respectively. We used the change in the ratio of real electrical resistance of the sensor upon air (R_a) and gas (R_g) to estimate the gas response ($\beta = R_a/R_g$). The response and recovery time are defined as the time to achieve 90% of total resistance changes by switching the sensor in target gas and air, respectively. During the test of sensing performance, the relative humidity of the atmosphere was about 30%.

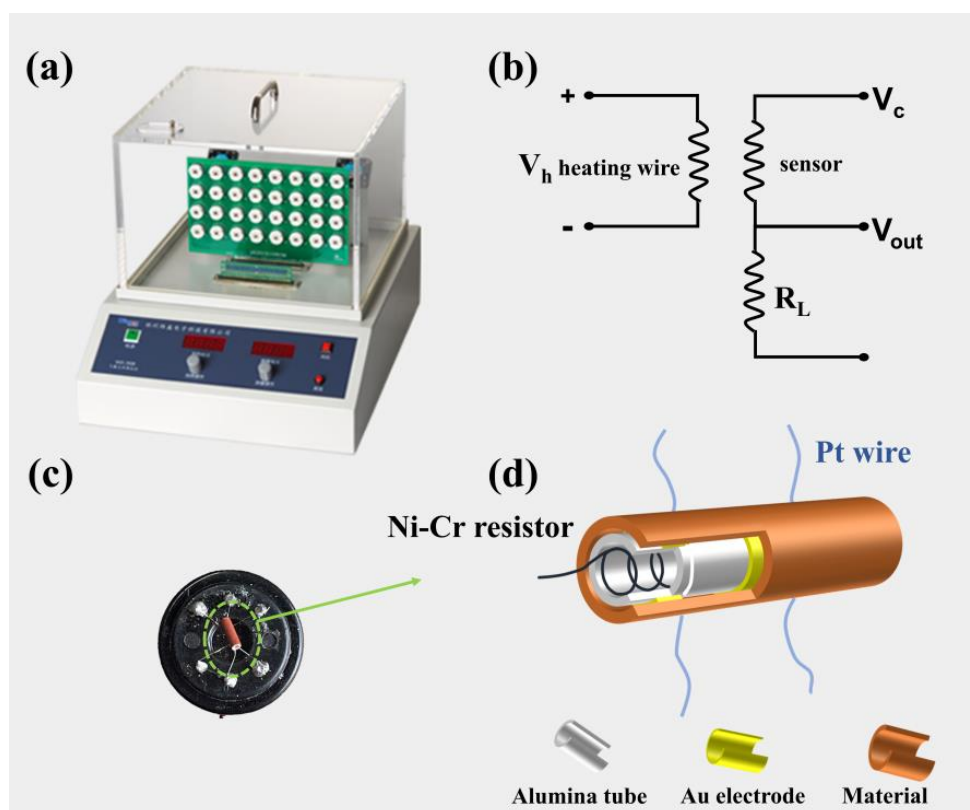


Figure 1. (a) The WS–30 gas–sensing measurement system, (b) basic test circuit, (c) photo of a gas sensor, and (d) schematic illustration of a gas sensor.

3. Results and Discussion

3.1. Morphology and Structure

The precursors of Fe-alkoxides were synthesized via a solvothermal method and then annealed in air at different temperatures including 350 °C, 400 °C and 450 °C to form pure-phase α -Fe₂O₃ and γ -Fe₂O₃, and the mixed-phase α/γ -Fe₂O₃. The synthesis procedure, as illustrated in Figure 2, involves a solvent of EG and CTAB as a surfactant. Initially, the EG molecules reduced Fe³⁺ to form Fe²⁺ ions. In addition, EG molecules coordinate with Fe²⁺ ions to form an iron alkoxide complex. Urea was further added to provide OH⁻ ions through hydrolysis, which neutralize the by-product of H⁺ to favor the coordination reaction [28,31]. Under the assistance of CTAB, the nucleation and growth of Fe-alkoxides begin to form nanosheets. With the prolongation in reaction time, these nanosheets could further self-assemble into three-dimensional flower-like microspheres to minimize the free energy of nanostructures. The XRD result of the Fe-alkoxides in Figure 3a shows a strong diffraction peak around 11° along with a weak peak at 18°, which matches well with the reported results [32,33]. Subsequently, we investigated the effects of calcination temperature on the crystal phase and morphology of products. The Fe-alkoxides were further thermally transformed into pure α -Fe₂O₃, γ -Fe₂O₃ and especially their mixed phase of α/γ -Fe₂O₃ for high-sensing performance towards acetone.

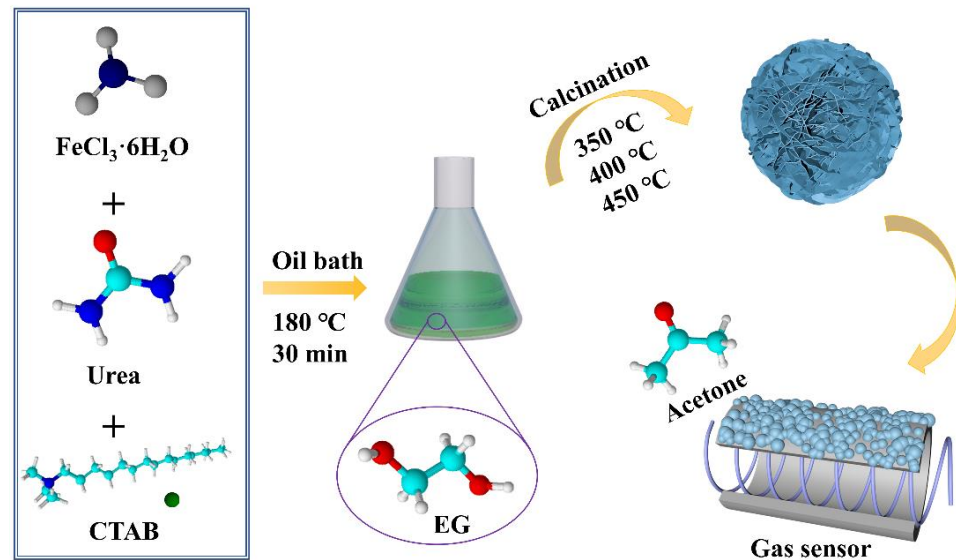


Figure 2. Schematic diagram of the synthesis procedure of hierarchical Fe₂O₃ micro-flower.

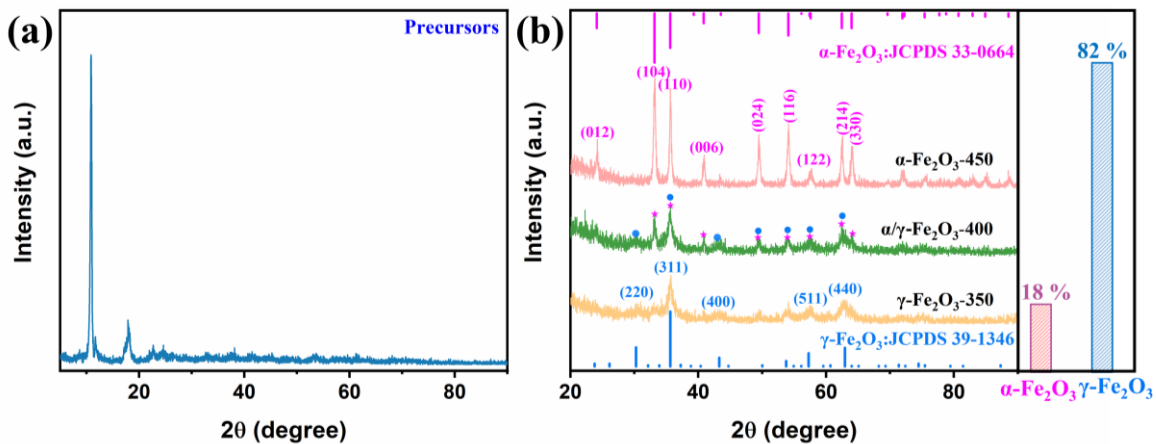


Figure 3. XRD characterizations of (a) the Fe-alkoxides, (b) γ -Fe₂O₃-350, α/γ -Fe₂O₃-400 and α -Fe₂O₃-450.

X-ray diffraction (XRD) analysis was performed to investigate the crystallinity after calcination. As displayed in Figure 3b, the phase of products is strongly dependent on the annealing temperature. Obviously, the sample calcined at 350 °C matches perfectly with the standard pattern of a maghemite (γ -Fe₂O₃) crystalline structure (JCPDS: 39-1346). This phase possesses a rhombic-centered corundum-type hexagonal structure which is associated with Fe(III) ions for two-thirds of the octahedral positions and a tight oxygen lattice [34]. At the higher temperature of 450 °C, all detectable peaks are indexed to the hematite (α -Fe₂O₃) by comparing with JCPDS: 33-0664. The γ -Fe₂O₃ shows an anti-spinel-type cubic crystal structure, in which the Fe(III) occupy tetrahedral and octahedral positions [34]. Interestingly, the mixed phase of α/γ -Fe₂O₃-400 is obtained when the annealing temperature is 400 °C. Using MDI Jade refinement analysis, the proportions of γ -Fe₂O₃ and α -Fe₂O₃ in the α/γ -Fe₂O₃-400 are estimated to be 82% and 18%, indicating the partial conversion of γ -Fe₂O₃ to α -Fe₂O₃ with increase in temperature. Moreover, the diffraction peaks of α -Fe₂O₃ show smaller half-widths and strong diffraction intensities, indicating that the higher calcination temperature promotes the crystallinity of the products.

The morphology of precursor and samples calcined at 400 °C (α/γ -Fe₂O₃-400) was observed by FESEM. As displayed in Figure 4a,c, the Fe-alkoxides are flower-like architectures in shape with smooth surfaces, which are assembled from a bunch of nanosheets. After being annealed at 400 °C in air, the overall flower-like structures of the precursor are preserved, as shown in Figure 4b,d. However, the rough nanosheet surface is observed due to the decomposition of organic parts in Fe-alkoxides. To characterize the microstructure of α/γ -Fe₂O₃ in detail, TEM analyses were carried out. As shown in Figure 5, typical α/γ -Fe₂O₃ flower-like structures are 1–2 μ m in size and the nanosheets are approximately 40 nm in thickness. Meanwhile, HRTEM images of the α/γ -Fe₂O₃-400 (Figure 5d,e) show a lattice spacing of 0.295 nm, 0.482 nm and 0.592 nm, corresponding to the (220), (111), and (110) planes of γ -Fe₂O₃, respectively. Furthermore, the clear lattice spacing of 0.270 nm and 0.252 nm are attributed to the α -Fe₂O₃ in the (104) and (110) planes. Importantly, the interface derived from the dual phase of α -Fe₂O₃ and γ -Fe₂O₃ can be clearly seen in Figure 5d,e, which further proves the coexistence of α -Fe₂O₃ and γ -Fe₂O₃. Furthermore, the selected area electron diffraction (SAED) in Figure 5f illustrates the polycrystalline nature of the mixed phase of α/γ -Fe₂O₃. The diffraction pattern consists of polycrystalline diffraction rings, which matches well with the (220), (111), (311) and (520) crystal planes of γ -Fe₂O₃, and the (042), (113) and (220) crystal planes of α -Fe₂O₃, respectively. The compositional analysis of α/γ -Fe₂O₃-400 was investigated by EDS testing (Figure 5g–i), which more visually reveals the highly homogeneous distribution of Fe and O within the material.

In order to understand the conversion of Fe-alkoxides to Fe₂O₃, we studied the thermal decomposition procedure of the precursor by thermogravimetric analysis (TGA) and differential scanning calorimetry (DSC). In Figure 6a, a clear exothermic peak at 308 °C on the DSC curve is observed. Apart from the removal of residual water at low temperature, a big weight loss of 42.47% from 240 °C to 400 °C occurs, corresponding to the decomposition of Fe-alkoxides and the formation of Fe₂O₃. Furthermore, the N₂ adsorption–desorption isotherm was recorded to evaluate the specific surface area and pore structure of the flower-like Fe₂O₃ by taking α/γ -Fe₂O₃-400 as an example. As shown in Figure 6b, the isotherm of this sample can be classified as a type IV, with a small hysteresis loop with relative pressure ranging from 0.3–1.0. According to the International Union of Pure and Applied Chemistry (IUPAC) classification, this hysteresis loop belongs to the type H4 return line, indicating the presence of mesopores. Brunauer–Emmett–Teller (BET) gas adsorption measurements exhibit that the specific surface area and pore volume of the α/γ -Fe₂O₃ are 67.324 m²/g and 0.238 cc/g. The average Barrett–Joyner–Halenda (BJH) pore diameter verifies that the pores are mostly distributed around 3.406 nm. The loose interspaces in the flower-like structure with large BET surface area and suitable pore size distribution are beneficial to provide more active reaction sites and effective channels for acetone detection [35,36].

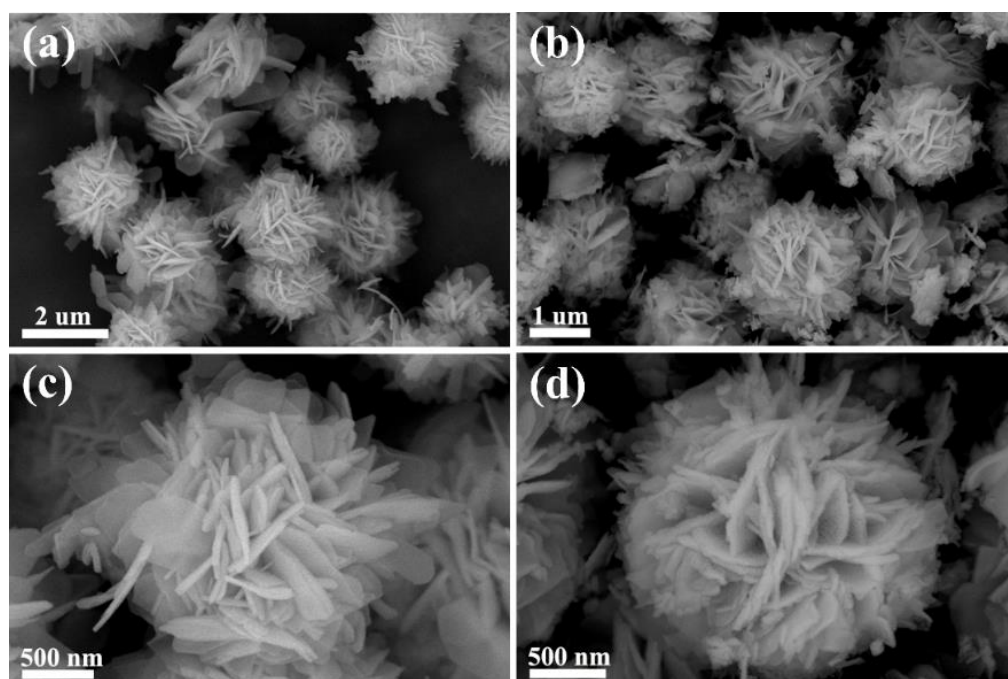


Figure 4. FESEM images of (a,c) Fe-alkoxides, and (b,d) the mixed phase of $\alpha/\gamma\text{-Fe}_2\text{O}_3\text{-400}$.

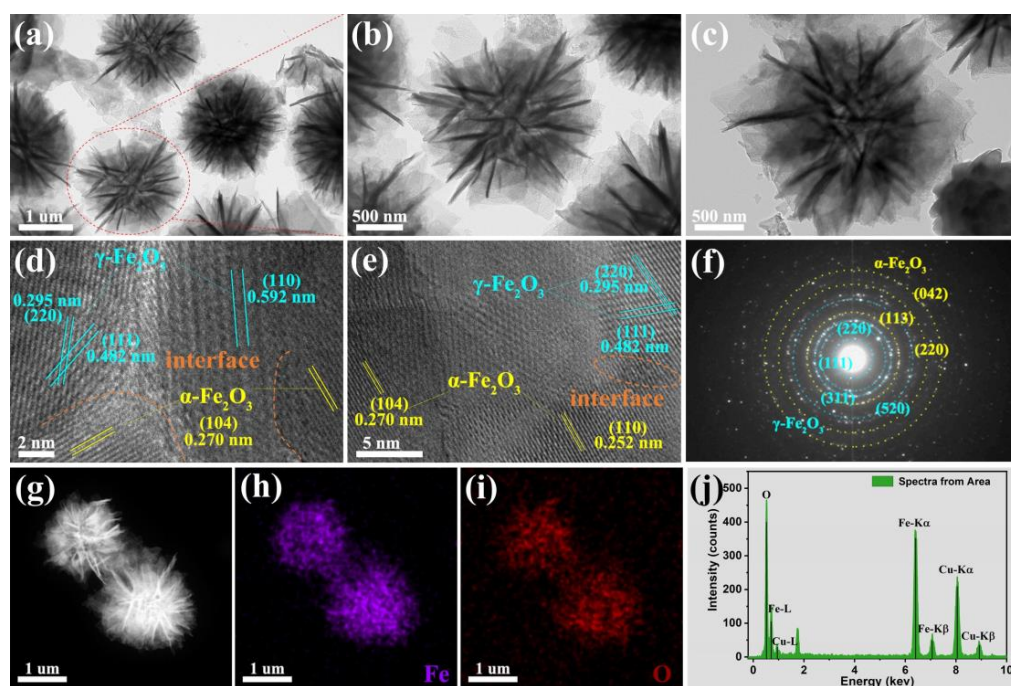


Figure 5. (a–c) TEM, (d,e) HRTEM, (f) SAED images, and EDS maps of (h) Fe, and (i) O for selected area of (g), and (j) the EDS spectra of $\alpha/\gamma\text{-Fe}_2\text{O}_3\text{-400}$.

X-ray photoelectron spectroscopy (XPS) was further used to study the chemical compositions and valance states of the elements in the mixed-phase $\alpha/\gamma\text{-Fe}_2\text{O}_3$. In the Fe 2p spectrum (Figure 6d), the peak at binding energy of 710.45 eV corresponds to Fe 2p_{3/2}. On the other hand, the peak at 723.96 eV is assigned to Fe 2p_{1/2}. These two major peaks are accompanied by satellite peaks centered at 718.67 eV and 732.45 eV, demonstrating the formation of the Fe₂O₃ [11,13]. After deconvolution of the O 1s spectrum (Figure 6c), two peaks are observed at binding energies of 529.76 eV and 530.97 eV, which are associated with the lattice oxygen atom (O_{lattice}) and the adsorbed oxygen (O_x⁻), respectively.

In particular, the adsorbed oxygen occupies 38.7% according to the area shared by the two peaks, which is active to react with acetone molecules to contribute a high response.

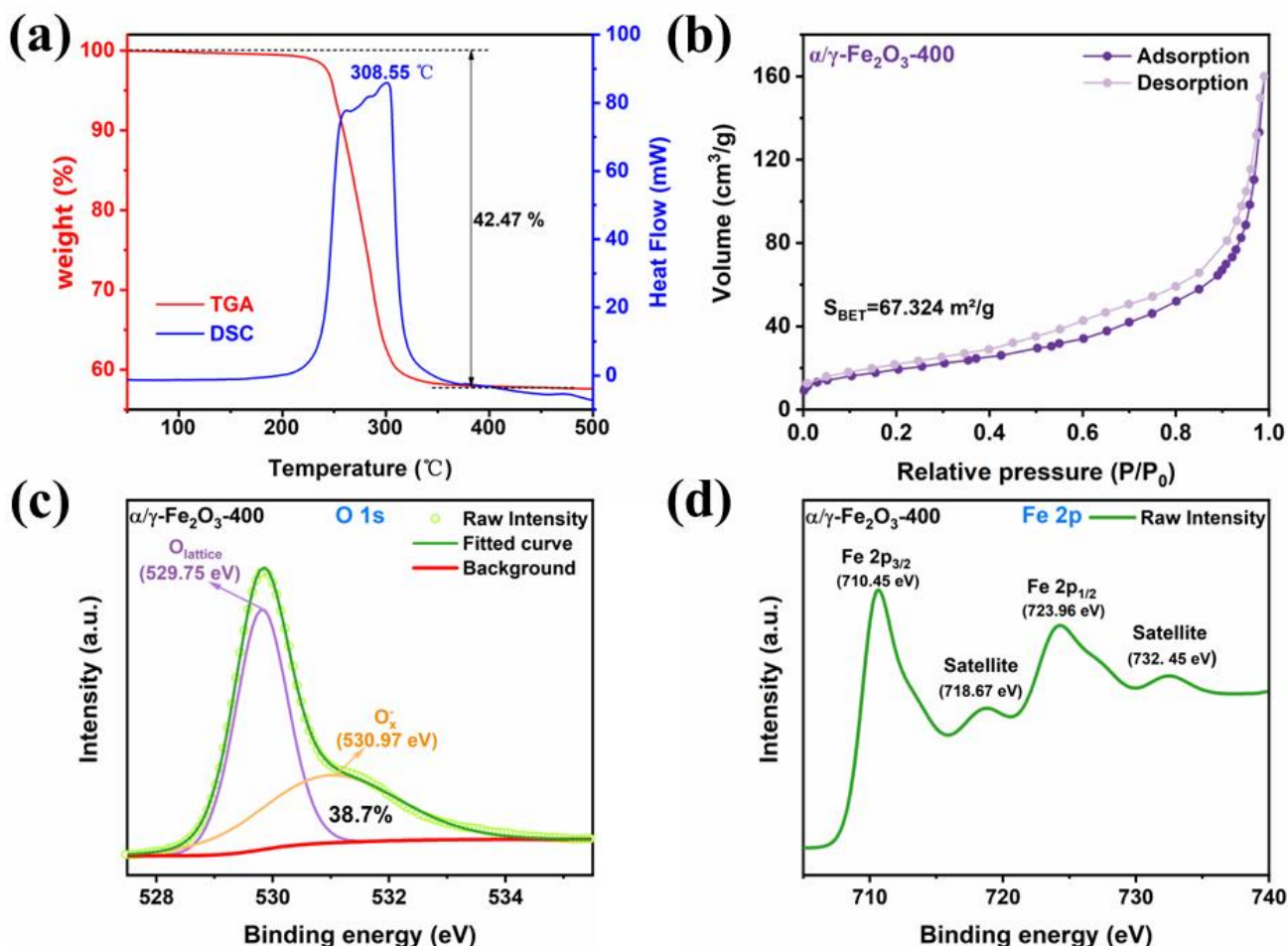


Figure 6. (a) TGA and DSC curves of precursors, and (b) nitrogen adsorption–desorption isotherms of mixed-phase $\alpha/\gamma\text{-Fe}_2\text{O}_3\text{-400}$, and high-resolution XPS spectra of $\alpha/\gamma\text{-Fe}_2\text{O}_3\text{-400}$, (c) O 1s and (d) Fe 2p.

3.2. Gas-Sensing Properties

For metal oxide semiconductors, sufficient thermal energy is generally needed to favor the surface chemisorption and reaction of gas molecules [37,38], which is an important parameter of a gas sensor. The responses of the sensors to 200 ppm acetone were measured at a series of temperatures from 120 °C to 220 °C, as shown in Figure 7a. At low working temperatures, the responses are very weak due to insufficient thermal energy. With the rising of the working temperature, the responses increase gradually and then reach a maximum of 163, 353, and 74 for the sensors based on $\gamma\text{-Fe}_2\text{O}_3\text{-350}$, $\alpha/\gamma\text{-Fe}_2\text{O}_3\text{-400}$ and $\alpha\text{-Fe}_2\text{O}_3\text{-450}$ at 160 °C. However, the decrease in sensor response is observed with further increments of the working temperature because of the accelerated gas desorption from the surface of sensing materials. Therefore, the temperature of 160 °C is selected as the best working temperature in the following tests.

Figure 7b,c are dynamic sensing responses to different concentrations from 0.5 to 200 ppm at 160 °C. Apparently, the responses of the sensors increase abruptly when they are exposed to acetone gas. After exposure in fresh air again, they recover to the initial value. The changes in responses to acetone concentration are plotted in Figure 7d. The mixed-phase $\alpha/\gamma\text{-Fe}_2\text{O}_3\text{-400}$ sensor performs better than the pure $\gamma\text{-Fe}_2\text{O}_3\text{-350}$ and $\alpha\text{-Fe}_2\text{O}_3\text{-450}$ at each concentration. For the $\alpha/\gamma\text{-Fe}_2\text{O}_3\text{-400}$ sensor, a linear relationship between responses and tested acetone concentrations from 50 to 200 ppm is fitted (inset

in Figure 7d) with $R^2 = 0.9992$. In addition, γ -Fe₂O₃-350, α/γ -Fe₂O₃-400 and α -Fe₂O₃-450 sensors show response values of 1.7, 2.25, and 1.2 to a low limit of detection (LOD) of 0.5 ppm acetone, demonstrating the quantitative detection for trace acetone, as shown in Figure 7b. The response and recovery times of α/γ -Fe₂O₃-400 are 22/13 s and 27/37 s to 200 ppm and 10 ppm acetone (Figure 7e,f). Furthermore, gas sensors must possess good repeatability and long-term stability and excellent selectivity towards practical gas detection. Figure 8a presents the reproducibility of gas sensors based on γ -Fe₂O₃-350, α/γ -Fe₂O₃-400 and α -Fe₂O₃-450 to 200 ppm acetone during five consecutive tests, which maintain the initial responses. For instance, the sensor based on α/γ -Fe₂O₃-400 shows a slight fluctuation in the range of 366–374, indicating an excellent reproducibility. Figure 8b shows long-term stability to 200 ppm acetone in 30 days, in which the response values remain relatively stable with standard deviations (S) of 5.89, 4.90 and 5.96 for γ -Fe₂O₃-350, α/γ -Fe₂O₃-400 and α -Fe₂O₃-450 to 200 ppm acetone. The selectivity of our sensors has also been evaluated, as shown in Figure 8c. Some typical VOC gases including acetone, isopropanol, ethanol, methanol, toluene, benzene, formaldehyde and ammonia were tested at 160 °C with a concentration of 200 ppm. It is obvious that all three different sensors show a pronounced response to acetone over other gases, which is determined by the different stability and activity of the gases. Especially, the response of the α/γ -Fe₂O₃-400 gas sensor is highest, which is probably correlated with the mixed phase. Table 1 lists the acetone-sensing properties of α/γ -Fe₂O₃-400 prepared in this work as well as other recent reports on α -Fe₂O₃ and γ -Fe₂O₃. Numerous reports show a higher optimum working temperature and lower response. Indeed, our mixed phase of α/γ -Fe₂O₃ exhibits a comparable sensing performance to acetone detection.

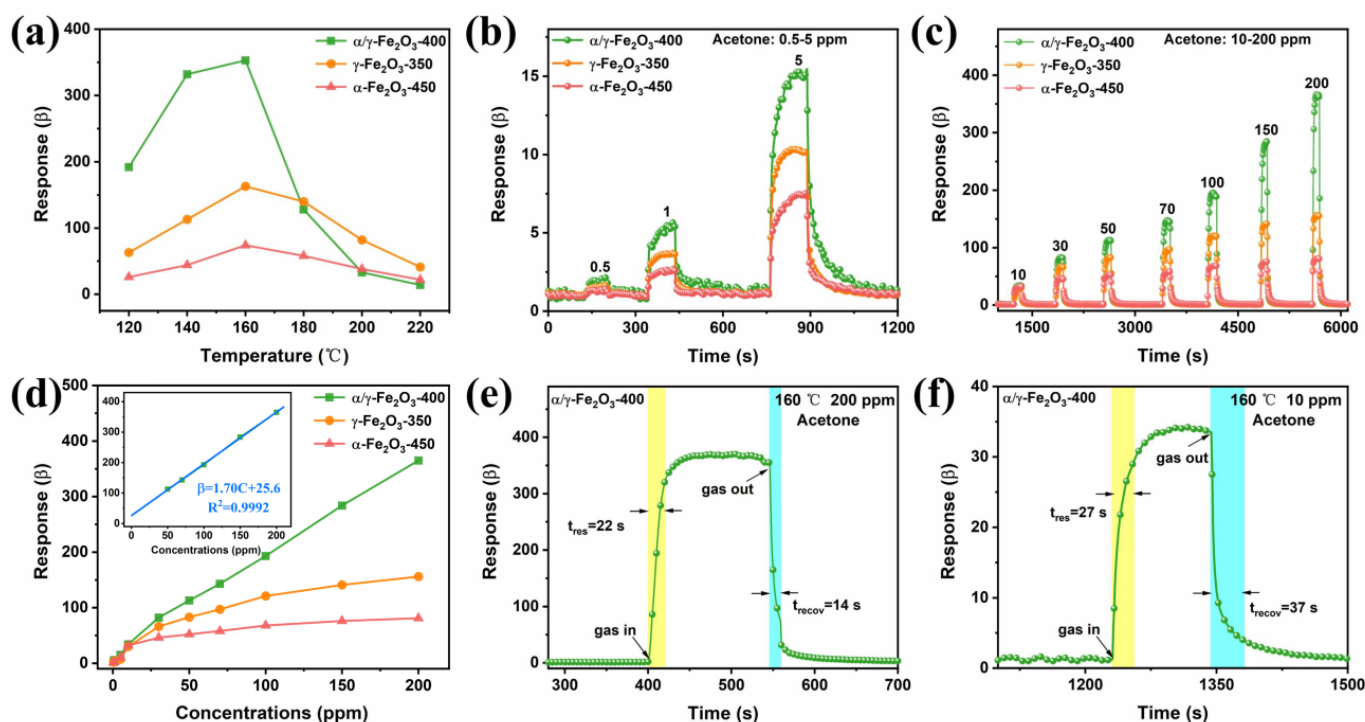


Figure 7. (a) Temperature-dependent responses of the gas sensors based on γ -Fe₂O₃-350, α/γ -Fe₂O₃-400 and α -Fe₂O₃-450 to 200 ppm, (b,c) response–recovery curves of the gas sensors to various acetone concentrations from 0.5 ppm to 200 ppm, (d) responses as a function of acetone concentration (inset is the linear relationship between the responses and concentration of the α/γ -Fe₂O₃-400), response and recovery time of α/γ -Fe₂O₃-400 to (e) 200 ppm acetone and (f) 10 ppm acetone. All sensing properties were tested at optimal operating temperature of 160 °C.

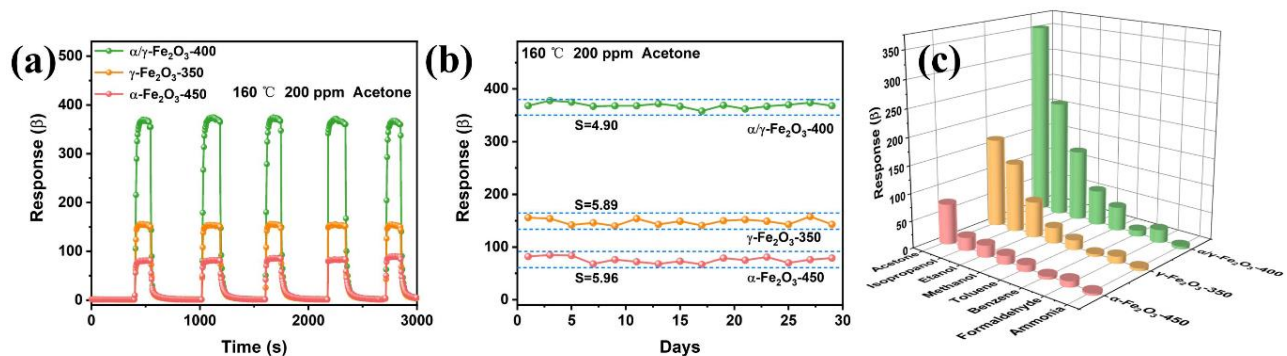


Figure 8. (a) Repeatability response–recovery curves of gas sensors based on γ -Fe₂O₃-350, α/γ -Fe₂O₃-400 and α -Fe₂O₃-450 over five cycles of exposure to 200 ppm acetone, (b) Long-term stability of gas sensors to 200 ppm acetone at 160 °C (S represents standard deviation), and (c) a comparison of the response for gas sensors towards 200 ppm different gases.

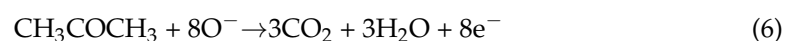
Table 1. Comparison of reported gas sensor based on α -Fe₂O₃ and γ -Fe₂O₃ to acetone.

Materials	T (°C)	C (ppm)	Response (β)	t _{res} /t _{rec} (s)	LOD	Ref.
Porous α -Fe ₂ O ₃	300	100	26.3	6/<100	10	[39]
Nanorods α -Fe ₂ O ₃	280	100	32.5	0.4/2.4	10	[40]
Nanoparticles α -Fe ₂ O ₃	340	100	9.1	–	5	[22]
Nanospheres α -Fe ₂ O ₃	170	100	16	2/50	0.1	[41]
Microrods γ -Fe ₂ O ₃	220	100	125.5	0.9/15	10	[24]
Nanocubes γ -Fe ₂ O ₃	350	100	161	–	10	[42]
Flower-like α/γ -Fe ₂ O ₃	160	200	353	22/14	0.5 ppm	This work

As reported, the gas-sensing mechanism for metal oxide-based sensors usually arises from the surface chemical reaction of target gas molecules, leading to the change in resistance [43,44]. In our work, when n-type Fe₂O₃ materials are exposed in air, the absorbed oxygen molecules on the surface will capture electrons from the conduction band of Fe₂O₃ to generate active oxygen ions of O₂[−], O[−] and O^{2−} at a certain temperature (as shown in Figure 9a and Equations (2)–(5)) [45,46]. The absorbed oxygen has been confirmed by the above XPS measurements.



For an n-type semiconductor, the loss of electrons produces a high resistance by forming an electron depletion layer. When the gas sensor is exposed to acetone atmosphere, the reaction between these oxygen species and acetone molecules leads to the release of the captured electrons. As a result, the increase in electrons in the conduction band of Fe₂O₃ leads to a decrease in the electron depletion layer. The supposed chemical reaction is expressed as follows [47,48]:



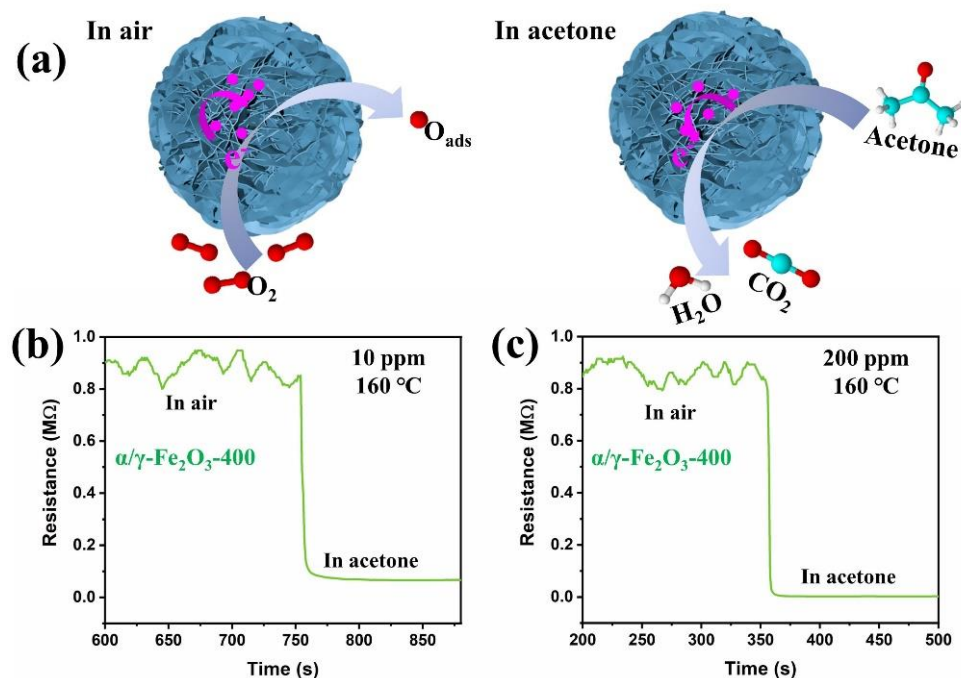


Figure 9. (a) Schematic illustration of the acetone-sensing mechanism, and the real resistance changes in $\alpha/\gamma\text{-Fe}_2\text{O}_3\text{-400}$ gas sensor to acetone with a concentration of (b) 10 ppm and (c) 200 ppm at 160 °C.

This process will give rise to a big change in resistance and thus endows a high response. For instance, the real resistance of the $\alpha/\gamma\text{-Fe}_2\text{O}_3\text{-400}$ gas sensor changed from 0.89 M Ω in air to 0.0685 M Ω and 0.0025 M Ω in 10 ppm and 200 ppm acetone, as shown in Figure 9b,c. The excellent gas-sensing performance of mixed-phase $\alpha/\gamma\text{-Fe}_2\text{O}_3$ for acetone detection is ascribed to the intrinsic nature of Fe_2O_3 unique nanosheets' assembled hierarchical structure, and the formation of a dual-phase interface. Firstly, the different valences of iron ions in Fe^{2+} and Fe^{3+} could favor the transfer of electrons [24]. The merits of a large surface area with a large number of active sites is beneficial for the accommodation of more oxygen molecules and acetone gas molecules, which promotes the reaction to produce a large change in resistance. In addition, the interconnection of nanosheets could form abundant inner space to increase the pathway for gas diffusion. Last but not least, due to the difference in the crystal structure of $\gamma\text{-Fe}_2\text{O}_3$ and $\alpha\text{-Fe}_2\text{O}_3$, the rich defects may be introduced by mixing them to form a dual-phase structure [49]. Furthermore, the boundary between $\gamma\text{-Fe}_2\text{O}_3$ and $\alpha\text{-Fe}_2\text{O}_3$ creates a large amount of phase heterojunction interface, which will be beneficial for improving the diffusion of charge carriers. Therefore, the mixed-phase $\alpha/\gamma\text{-Fe}_2\text{O}_3$ exhibits a higher gas-sensing performance over the counterparts of single-phase of $\gamma\text{-Fe}_2\text{O}_3$ and $\alpha\text{-Fe}_2\text{O}_3$ for acetone detection.

4. Conclusions

In this work, we reported the synthesis of Fe-alkoxides via a facile solvothermal method, which further converts into single $\gamma\text{-Fe}_2\text{O}_3$ and $\alpha\text{-Fe}_2\text{O}_3$ as well as the mixed-phase $\alpha/\gamma\text{-Fe}_2\text{O}_3$ depending on the calcination temperature. The hierarchical structure is assembled by a bunch of nanosheets, which provides a large surface area and number of channels for gas molecules reaction and diffusion. Compared with the single phases of $\gamma\text{-Fe}_2\text{O}_3$ and $\alpha\text{-Fe}_2\text{O}_3$, the mixed-phase $\alpha/\gamma\text{-Fe}_2\text{O}_3$ sensor shows a high response of 353 to 200 ppm acetone at 160 °C with a fast response and recovery time of 22/14 s, good selectivity and long-term stability. Importantly, a linear relationship between responses and the acetone concentration from 50 to 200 ppm is fitted for the $\alpha/\gamma\text{-Fe}_2\text{O}_3$ sensor, making it more practical for application. The present work offers a new vision of the crystalline-phase regulation of Fe_2O_3 from Fe-alkoxides to improve the sensing properties for effective

acetone detection. However, it is necessary to note that more work should be done to extend the current findings for real diagnostic use in the future.

Author Contributions: Conceptualization, C.D.; methodology, R.T.; formal analysis, H.T.; funding acquisition, G.C. and H.G.; writing—original draft preparation, R.T.; writing—review and editing, C.D. and Z.Y. All authors have read and agreed to the published version of the manuscript.

Funding: Financial support from the National Natural Science Foundation of China (22165032), and the Application Basic Research Fund of Yunnan Province (2019FB129, and 202301AT070207) and the Major Science and Technology Project of Precious Metal Materials Genetic Engineering in Yunnan Province (2019ZE001-6) is greatly appreciated. The authors acknowledge the Advanced Analysis and Measurement Center of Yunnan University for the sample testing service.

Data Availability Statement: The data that support the findings of this study are available within this article.

Conflicts of Interest: The authors declare no conflict of interest.

References

1. Amiri, V.; Roshan, H.; Mirzaei, A.; Neri, G.; Ayesh, A.I. Nanostructured metal oxide-based acetone gas sensors: A review. *Sensors* **2020**, *20*, 3096. [[CrossRef](#)] [[PubMed](#)]
2. Broza, Y.Y.; Vishinkin, R.; Barash, O.; Nakhleh, M.K.; Haick, H. Synergy between nanomaterials and volatile organic compounds for non-invasive medical evaluation. *Chem. Soc. Rev.* **2018**, *47*, 4781–4859. [[CrossRef](#)]
3. Baharuddin, A.A.; Ang, B.C.; Haseeb, A.S.M.A.; Wong, Y.C.; Wong, Y.H. Advances in chemiresistive sensors for acetone gas detection. *Mater. Sci. Semicond. Process.* **2019**, *103*, 104616. [[CrossRef](#)]
4. Moon, Y.K.; Kim, K.B.; Jeong, S.-Y.; Lee, J.-H. Designing oxide chemiresistors for detecting volatile aromatic compounds: Recent progresses and future perspectives. *Chem. Commun.* **2022**, *58*, 5439–5454. [[CrossRef](#)] [[PubMed](#)]
5. Mo, R.; Han, D.; Yang, C.; Tang, J.; Wang, F.; Li, C. MOF-derived porous Fe₂O₃ nanocubes combined with reduced graphene oxide for n-butanol room temperature gas sensing. *Sens. Actuators B Chem.* **2021**, *330*, 129326. [[CrossRef](#)]
6. Guo, Y.; Tian, X.; Wang, X.; Sun, J. Fe₂O₃ nanomaterials derived from prussian blue with excellent H₂S sensing properties. *Sens. Actuators B Chem.* **2019**, *293*, 136–143. [[CrossRef](#)]
7. Wang, H.; Yan, L.; Li, S.; Li, Y.; Liu, L.; Du, L.; Duan, H.; Cheng, Y. Acetone sensors based on microsheet-assembled hierarchical Fe₂O₃ with different Fe³⁺ concentrations. *Appl. Phys. A* **2018**, *124*, 212. [[CrossRef](#)]
8. Park, S.; Cai, Z.; Lee, J.; Yoon, J.I.; Chang, S.-P. Fabrication of a low-concentration H₂S gas sensor using CuO nanorods decorated with Fe₂O₃ nanoparticles. *Mater. Lett.* **2016**, *181*, 231–235. [[CrossRef](#)]
9. Fan, K.; Guo, J.; Cha, L.; Chen, Q.; Ma, J. Atomic layer deposition of ZnO onto Fe₂O₃ nanoplates for enhanced H₂S sensing. *J. Alloys Compd.* **2017**, *698*, 336–340. [[CrossRef](#)]
10. Jayababu, N.; Poloju, M.; Ramana Reddy, M.V. Facile synthesis of SnO₂-Fe₂O₃ core-shell nanostructures and their 2-methoxyethanol gas sensing characteristics. *J. Alloys Compd.* **2019**, *780*, 523–533. [[CrossRef](#)]
11. Zhang, S.; Song, P.; Liu, M.; Zheng, Y.; Wang, Q. Metal-organic framework-derived In-doped Fe₂O₃ spindles with enhanced acetone gas sensing performance. *Inorg. Chem. Commun.* **2022**, *142*, 109658. [[CrossRef](#)]
12. Chen, L.; Song, Y.; Yu, Q.; Dong, H.; Pan, C.; Wang, D.; Liu, J.; Chen, X. High-performance acetone sensor based on electrospun Tb-doped α -Fe₂O₃ nanotubes. *Ceram. Int.* **2022**, *48*, 26828–26835. [[CrossRef](#)]
13. Zhang, S.; Yang, M.; Liang, K.; Turak, A.; Zhang, B.; Meng, D.; Wang, C.; Qu, F.; Cheng, W.; Yang, M. An acetone gas sensor based on nanosized Pt-loaded Fe₂O₃ nanocubes. *Sens. Actuators B Chem.* **2019**, *290*, 59–67. [[CrossRef](#)]
14. Yang, C.; Yang, Y.; Zhang, C.; Yu, H.; Wang, T.; Shi, K.; Zhang, Z.; Wang, D.; Dong, X. High selectivity of Ag-doped Fe₂O₃ hollow nanofibers in H₂S detection at room operating temperature. *Sens. Actuators B Chem.* **2021**, *341*, 129919. [[CrossRef](#)]
15. Liu, X.; Zhang, J.; Wu, S.; Yang, D.; Liu, P.; Zhang, H.; Wang, S.; Yao, X.; Zhu, G.; Zhao, H. Single crystal α -Fe₂O₃ with exposed {104} facets for high performance gas sensor applications. *RSC Adv.* **2012**, *2*, 6178–6184. [[CrossRef](#)]
16. Ma, Y.; Yang, J.; Yuan, Y.; Zhao, H.; Shi, Q.; Zhang, F.; Pei, C.; Liu, B.; Yang, H. Enhanced gas sensitivity and sensing mechanism of network structures assembled from α -Fe₂O₃ nanosheets with exposed {104} facets. *Langmuir* **2017**, *33*, 8671–8678. [[CrossRef](#)]
17. Ouyang, J.; Pei, J.; Kuang, Q.; Xie, Z.; Zheng, L. Supersaturation-controlled shape evolution of α -Fe₂O₃ nanocrystals and their facet-dependent catalytic and sensing properties. *ACS Appl. Mater. Inter.* **2014**, *6*, 12505–12514. [[CrossRef](#)]
18. Sui, N.; Cao, S.; Zhang, P.; Zhou, T.; Zhang, T. The effect of different crystalline phases of In₂O₃ on the ozone sensing performance. *J. Hazard. Mater.* **2021**, *418*, 126290. [[CrossRef](#)]
19. Hu, D.; Han, B.; Deng, S.; Feng, Z.; Wang, Y.; Popovic, J.; Nuskol, M.; Wang, Y.; Djerdj, I. Novel mixed phase SnO₂ nanorods assembled with SnO₂ nanocrystals for enhancing gas-sensing performance toward isopropanol gas. *J. Phys. Chem. C* **2014**, *118*, 9832–9840. [[CrossRef](#)]
20. Wang, M.; Hou, T.; Shen, Z.; Zhao, X.; Ji, H. MOF-derived Fe₂O₃: Phase control and effects of phase composition on gas sensing performance. *Sens. Actuators B Chem.* **2019**, *292*, 171–179. [[CrossRef](#)]

21. Xue, Y.; Wang, Y. A review of the α -Fe₂O₃ (hematite) nanotube structure: Recent advances in synthesis, characterization, and applications. *Nanoscale* **2020**, *12*, 10912–10932. [[CrossRef](#)] [[PubMed](#)]
22. Liang, S.; Li, J.; Wang, F.; Qin, J.; Lai, X.; Jiang, X. Highly sensitive acetone gas sensor based on ultrafine α -Fe₂O₃ nanoparticles. *Sens. Actuators B Chem.* **2017**, *238*, 923–927. [[CrossRef](#)]
23. Zhuang, Z.; Zhang, L.; Huang, C.; Wang, X.; Guo, H.; Thomas, T.; Qu, F.; Wang, P.; Yang, M. A dimethyl disulfide gas sensor based on nanosized Pt-loaded tetrakaidecahedral α -Fe₂O₃ nanocrystals. *Nanotechnology* **2022**, *33*, 405502. [[CrossRef](#)] [[PubMed](#)]
24. Song, Z.; Chen, H.; Bao, S.; Xie, Z.; Kuang, Q.; Zheng, L. Nanosheet-assembled, hollowed-out hierarchical γ -Fe₂O₃ microrods for high-performance gas sensing. *J. Mater. Chem. A* **2020**, *8*, 3754–3762. [[CrossRef](#)]
25. Zahmouli, N.; Hjiri, M.; Leonardi, S.G.; El Mir, L.; Neri, G.; Iannazzo, D.; Espro, C.; Aida, M.S. High performance Gd-doped γ -Fe₂O₃ based acetone sensor. *Mater. Sci. Semicond. Process.* **2020**, *116*, 105154. [[CrossRef](#)]
26. Dang, S.; Zhu, Q.-L.; Xu, Q. Nanomaterials derived from metal–organic frameworks. *Nat. Rev. Mater.* **2017**, *3*, 17075. [[CrossRef](#)]
27. Tang, B.; Wang, G.; Zhuo, L.; Ge, J.; Cui, L. Facile route to α -FeOOH and α -Fe₂O₃ nanorods and magnetic property of α -Fe₂O₃ nanorods. *Inorg. Chem.* **2006**, *45*, 5196–5200. [[CrossRef](#)]
28. Liu, X.; Gong, M.; Deng, S.; Zhao, T.; Zhang, J.; Wang, D. Recent advances on metal alkoxide-based electrocatalysts for water splitting. *J. Mater. Chem. A* **2020**, *8*, 10130–10149. [[CrossRef](#)]
29. Dong, C.; Tian, R.; Zhang, Y.; Liu, K.; Chen, G.; Guan, H.; Yin, Z. MOF-on-MOF nanoarchitecturing of Fe₂O₃@ZnFe₂O₄ radial-heterospindles towards multifaceted superiorities for acetone detection. *Chem. Eng. J.* **2022**, *442*, 136094. [[CrossRef](#)]
30. Dong, C.; Tian, R.; Qu, H.; Tan, H.; Chen, G.; Guan, H.; Yin, Z. Anchoring Pt particles onto mesoporous ZnO holey cubes for triethylamine detection with multifaceted superiorities. *Small* **2023**, *19*, 2300756. [[CrossRef](#)] [[PubMed](#)]
31. Li, X.; Zhang, B.; Ju, C.; Han, X.; Du, Y.; Xu, P. Morphology-controlled synthesis and electromagnetic properties of porous Fe₃O₄ nanostructures from Iron Alkoxide Precursors. *J. Phys. Chem. C* **2011**, *115*, 12350–12357. [[CrossRef](#)]
32. Zhong, L.-S.; Hu, J.-S.; Liang, H.-P.; Cao, A.-M.; Song, W.; Wan, L.-J. Self-assembled 3D flowerlike iron oxide nanostructures and their application in water treatment. *Adv. Mater.* **2006**, *18*, 2426–2431. [[CrossRef](#)]
33. Ma, X.-H.; Feng, X.-Y.; Song, C.; Zou, B.-K.; Ding, C.-X.; Yu, Y.; Chen, C.-H. Facile synthesis of flower-like and yarn-like α -Fe₂O₃ spherical clusters as anode materials for lithium-ion batteries. *Electrochim. Acta* **2013**, *93*, 131–136. [[CrossRef](#)]
34. Machala, L.; Tuček, J.; Zbořil, R. Polymorphous transformations of nanometric iron(III) oxide: A review. *Chem. Mater.* **2011**, *23*, 3255–3272. [[CrossRef](#)]
35. Song, H.; Yan, S.; Yao, Y.; Xia, L.; Jia, X.; Xu, J. 3D α -Fe₂O₃ nanorods arrays@graphene oxide nanosheets as sensing materials for improved gas sensitivity. *Chem. Eng. J.* **2019**, *370*, 1331–1340. [[CrossRef](#)]
36. Huang, D.; Li, H.; Wang, Y.; Wang, X.; Cai, L.; Fan, W.; Chen, Y.; Wang, W.; Song, Y.; Han, G.; et al. Assembling a high-performance acetone sensor based on MOFs-derived porous bi-phase α -/ γ -Fe₂O₃ nanoparticles combined with Ti₃C₂T_x nanosheets. *Chem. Eng. J.* **2022**, *428*, 131377. [[CrossRef](#)]
37. Qu, F.; Zhou, X.; Zhang, B.; Zhang, S.; Jiang, C.; Ruan, S.; Yang, M. Fe₂O₃ nanoparticles-decorated MoO₃ nanobelts for enhanced chemiresistive gas sensing. *J. Alloys Compd.* **2019**, *782*, 672–678. [[CrossRef](#)]
38. Qu, F.; Jiang, H.; Yang, M. Designed formation through a metal organic framework route of ZnO/ZnCo₂O₄ hollow core–shell nanocages with enhanced gas sensing properties. *Nanoscale* **2016**, *8*, 16349–16356. [[CrossRef](#)]
39. Geng, W.; Ge, S.; He, X.; Zhang, S.; Gu, J.; Lai, X.; Wang, H.; Zhang, Q. Volatile organic compound gas-sensing properties of bimodal porous α -Fe₂O₃ with ultrahigh sensitivity and fast response. *ACS Appl. Mater. Inter.* **2018**, *10*, 13702–13711. [[CrossRef](#)]
40. Tan, J.; Huang, X. Ultra-thin nanosheets-assembled hollowed-out hierarchical α -Fe₂O₃ nanorods: Synthesis via an interface reaction route and its superior gas sensing properties. *Sens. Actuators B Chem.* **2016**, *237*, 159–166. [[CrossRef](#)]
41. Wang, P.; Zhang, X.; Gao, S.; Cheng, X.; Sui, L.; Xu, Y.; Zhao, X.; Zhao, H.; Huo, L. Superior acetone sensor based on single-crystalline α -Fe₂O₃ mesoporous nanospheres via [C₁₂mim][BF₄]-assistant synthesis. *Sens. Actuators B Chem.* **2017**, *241*, 967–977. [[CrossRef](#)]
42. Van Minh Hai, H.; Cuong, N.D.; Mai, H.D.; Long, H.T.; Phuong, T.Q.; Dang, T.K.; Thong, L.V.; Viet, N.N.; Van Hieu, N. Superior detection and classification of ethanol and acetone using 3D ultra-porous γ -Fe₂O₃ nanocubes-based sensor. *Sens. Actuators B Chem.* **2022**, *362*, 131737. [[CrossRef](#)]
43. Ji, H.; Zeng, W.; Li, Y. Gas sensing mechanisms of metal oxide semiconductors: A focus review. *Nanoscale* **2019**, *11*, 22664–22684. [[CrossRef](#)]
44. Staerz, A.; Weimar, U.; Barsan, N. Current state of knowledge on the metal oxide based gas sensing mechanism. *Sens. Actuators B Chem.* **2022**, *358*, 131531. [[CrossRef](#)]
45. Zhang, W.; Fan, Y.; Yuan, T.; Lu, B.; Liu, Y.; Li, Z.; Li, G.; Cheng, Z.; Xu, J. Ultrafine tungsten oxide nanowires: Synthesis and highly selective acetone sensing and mechanism analysis. *ACS Appl. Mater. Inter.* **2020**, *12*, 3755–3763. [[CrossRef](#)] [[PubMed](#)]
46. Mane, A.A.; Moholkar, A.V. Effect of film thickness on NO₂ gas sensing properties of sprayed orthorhombic nanocrystalline V₂O₅ thin films. *Appl. Surf. Sci.* **2017**, *416*, 511–520. [[CrossRef](#)]
47. Liu, C.; Zhao, L.; Wang, B.; Sun, P.; Wang, Q.; Gao, Y.; Liang, X.; Zhang, T.; Lu, G. Acetone gas sensor based on NiO/ZnO hollow spheres: Fast response and recovery, and low (ppb) detection limit. *J. Colloid Interface Sci.* **2017**, *495*, 207–215. [[CrossRef](#)] [[PubMed](#)]

48. Fan, X.; Xu, Y.; Ma, C.; He, W. In-situ growth of Co_3O_4 nanoparticles based on electrospray for an acetone gas sensor. *J. Alloys Compd.* **2021**, *854*, 157234. [[CrossRef](#)]
49. Tian, R.; Gao, Z.; Chen, G.; Guan, H.; Dong, C.; Comini, E. Functionalized Pt nanoparticles between $\alpha/\gamma\text{-Fe}_2\text{O}_3$ and MXene for superior acetone sensing. *Sens. Actuators B Chem.* **2023**, *383*, 133584. [[CrossRef](#)]

Disclaimer/Publisher's Note: The statements, opinions and data contained in all publications are solely those of the individual author(s) and contributor(s) and not of MDPI and/or the editor(s). MDPI and/or the editor(s) disclaim responsibility for any injury to people or property resulting from any ideas, methods, instructions or products referred to in the content.